AWPL-10-25-3469

Hybrid Beam-Switching and Scanning Millimeter-Wave Array with Planar Luneburg Lenses

Xiaolian Mao, *Member, IEEE*, Qiang Chen, *Senior Member, IEEE*

***Abstract*—This letter presents a millimeter-wave (mm-wave) hybrid array that combines *H*-plane beam switching with planar Luneburg-lens elements and *E*-plane beam scanning based on phased-array concepts. Each element is implemented on a single-layer PCB, monolithically integrating a modified planar Luneburg lens with a grounded coplanar waveguide (GCPW) to substrate integrated waveguide (SIW) feed, improving integration into mm-wave circuits. The array operates over 26–32 GHz and provides ±60° *H*-plane and ±30° *E*-plane coverage with low scan loss. Compared to traditional lenses and phased arrays, it offers broadband, high gain, wide-angle coverage, and a simpler architecture, achieving an excellent performance–cost/power tradeoff while supporting deployment, maintenance, and mass production for future 6G communication systems.**

***Index Terms*—Beam switching, beam scanning, hybrid array, Luneburg lens, millimeter-wave, 6G.**

I. INTRODUCTION

Future 6G services, such as holographic communications, digital twins, and cloud VR, will impose stricter wireless requirements, demanding higher spectral efficiency at lower power levels. Given the limited deployment of millimeter-wave (mm-wave) in 5G and 6G systems, these systems must provide high gain, dynamic multibeam forming, and cost- and energy-efficient array architectures. Therefore, balancing beam performance with cost and power consumption is crucial. In scenarios such as vehicular communications, this balance naturally motivates a hybrid strategy: fixed-sector beam switching is adequate for slow lateral lane changes, while dynamic beam scanning (tracking) is necessary to maintain link quality during rapid longitudinal movement.

Phased arrays and lens antennas are two widely used multibeam solutions. Phased arrays offer dynamic wide-angle scanning, a low profile, and a lightweight design. However, they face issues such as feed network loss, limited bandwidth, structural complexity, and higher cost and power consumption. Conversely, lens antennas feature simple feeds, broad bandwidth, easy-to-construct structures, and low cost and power consumption. However, they are often large, have feeds separated from the lens body, and usually support only fixed sector beam switching [1]-[4]. A hybrid lens array combining beam switching with beam scanning provides a practical solution to these needs. All-metal lens arrays have been studied [5], [6]; however, they suffer from high surface roughness and conductor loss, and the air-filled waveguide structure is costly and challenging to integrate into mm-wave circuits. PCB-based lens arrays with periodic non-plated vias (NPVs) [7], [8] offer a low-cost alternative; however, these often require a large array aperture.

To address these challenges, this letter proposes a mm-wave hybrid beam-switching and scanning array based on planar Luneburg lenses. Numerous planar Luneburg lenses have been reported [9]-[16]; however, each has inherent limitations for mm-wave circuit-level integration. In this letter, a modified planar Luneburg lens is realized with periodic NPVs and excited through a grounded coplanar waveguide (GCPW)-to-substrate integrated waveguide (SIW) transition, enabling a fully integrated lens-feed design compatible with single-layer PCB fabrication. The proposed design offers broadband operation, wide-angle beam coverage, structural simplicity, and low cost and power consumption.

In this work, a modified planar Luneburg lens with periodic NPVs was designed, fabricated, and validated. Over 26−32 GHz, the measured feed-port reflection was less than −10 dB, and the mutual coupling was less than −15 dB. A ten-element array was evaluated through array synthesis using embedded-element radiation patterns at 30 GHz. The array achieved a peak gain of 22.2 dBi. Beam steering covered ±60° in the *H*-plane with scan loss less than 2.4 dB and ±30° in the *E*-plane with scan loss less than 2.9 dB, while sidelobe levels remained below −8 dB across all beams.

II. HYBRID ARRAY DESIGN

A. Hybrid Array Architecture

The proposed hybrid array comprises ten planar Luneburg lens antennas, each equipped with eleven feed ports. The elements are arranged as a one-dimensional, uniformly spaced linear array along the *y*-axis with an inter-element spacing of 6 mm. The radiating apertures are oriented toward the positive *z*-axis, as shown in Fig. 1. The hybrid array system includes the lens array, a switching matrix, a beamforming network (BFN), and the feeding network. This hybrid array features a brick-based design, with each planar lens operating independently or combining to form larger arrays, enabling modular expansion.

Manuscript received Oct. 23, 2025; accepted Nov. 7, 2025. This work was supported in part by JST SPRING, Grant Number JPMJSP2114, and in part by the National Institute of Information and Communications Technology (NICT), commissioned research Number 02201. (Corresponding author: Xiaolian Mao.)

Xiaolian Mao and Qiang Chen are with the Department of Communications Engineering, Tohoku University, Sendai 980-8579, Japan (e-mail: mao.xiaolian.r2@dc.tohoku.ac.jp; qiang.chen.a5@tohoku.ac.jp).

For *H*-plane (*x*–*z* plane) operation, the eleven feed ports of each lens are connected to the switching matrix, enabling port selection and beam switching over a ±60° range. For E-plane (y–z plane) operation, each lens is fed through an electronic phase shifter to realize beam scanning. In the *H*-plane, each lens produces a narrow beam; in the *E*-plane, the lens exhibits a wide beamwidth, and continuous scanning is achieved by controlling the excitation phase.

B. Single-Layer PCB Planar Luneburg Lens

A Luneburg lens converts a spherical wave launched from a point on its surface into a plane wave on the opposite side, enabling multibeam operation by switching among surface feed locations. The graded refractive index distribution is fundamental to its design. In practice, the permittivity and hence the effective refractive index can be tailored by drilling holes in a dielectric. For PCB implementations, a periodic array of NPVs in the copper-clad laminate enables controlled variation of the effective permittivity; the desired index profile is realized by specifying via diameters layer by layer [7]. Typical high-frequency laminates offer a minimum relative permittivity of about 2.0, which is insufficient to realize the full Luneburg index range (1.41–1.00) due to manufacturing constraints.

To address this limitation, a modified refractive index distribution is adopted to control the variation from the edge to the center within a range of 0.41. A RO4350B substrate ($\varepsilon_r = 3.66$, $\tan\delta = 0.0037$) is employed, yielding a refractive index distribution from 1.91 to 1.50. The modified refractive index profile [17] is

$$n(r) = \sqrt{2-(r/R)^2} + \sqrt{\varepsilon_r} - \sqrt{2}. \tag{1}$$

R is the external radius of the lens, r is the radial distance from a point inside the lens to its center, $n(r)$ is the refractive index, and ε_r is the substrate permittivity.

The dispersion curves of equivalent refractive index with via diameters were extracted in HFSS using the waveguide method. Over the 26–32 GHz range, the extracted dispersion curves are nearly dispersion-invariant, allowing the target profile to be maintained while selecting NPV diameters. The lens consists of 22 concentric layers with an overall radius of 32.25 mm. Due to fabrication limitations, via diameters are restricted to 0.3–1.2 mm; consequently, the achievable index range is approximately 1.91–1.55. Fig. 2(a) shows the equivalent and realized refractive indices versus the lens radius, with a maximum deviation of 0.05.

A GCPW-to-SIW transition is employed for feeding, which integrates seamlessly with the circuitry and lens structure. The GCPW impedance is readily controlled, facilitating a robust 50-Ω match between the SIW and a coaxial connector even on relatively thick substrates. A GCPW-to-SIW feed structure [18], [19] was designed and excited via an end-launch connector. The feed uses the same 1.524 mm substrate thickness as the lens and has a total length of 16.02 mm.

By integrating the lens with the GCPW-to-SIW feed, an 11-port planar Luneburg-lens element with two virtual ports is realized, as shown in Fig. 2(b). The Adjacent feed ports are spaced by 12°, providing ±60° coverage. Ports 1–11 map to Beams 1–11, respectively. To improve inter-port isolation, a shielding via fence is placed along the lens periphery between adjacent feeds. To reduce free-space reflections, a matching layer with permittivity equal to that of the lens's outermost layer is added at the radiating aperture. The matching layer thickness is 6 mm, aligned with the element spacing for array-level integration. To keep the assembly compact, the housing does not extend radially beyond the feeding length. Considering this constraint and after HFSS optimization, the radial length of the matching layer was set to 13.5 mm. This configuration allows for a monolithic 3D-printed matching layer and enclosure.

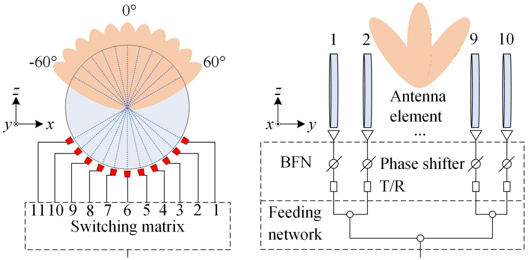

(a) (b)

Fig. 1. Block diagram of the proposed hybrid (a) beam-switching and (b) scanning array.

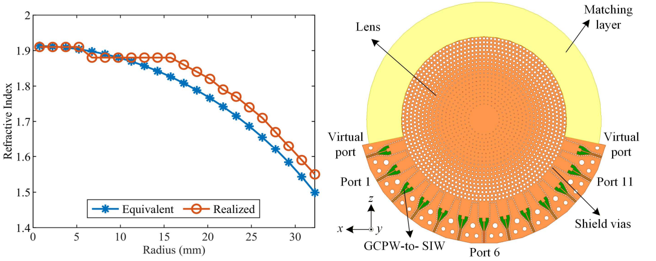

(a) (b)

Fig. 2. (a) Equivalent and realized refractive index versus lens radius. (b) Top view of the planar Luneburg lens with GCPW-to-SIW feeds.

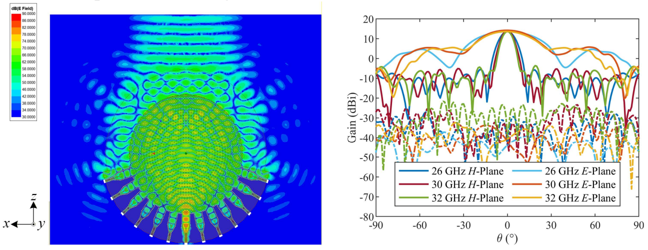

(a) (b)

Fig. 3. (a) Simulated *H*-plane magnitude of the electric field at 30 GHz for Port 6. (b) Simulated radiation patterns for Port 6 at 26 GHz, 30 GHz, and 32 GHz. (Co-polarization (Co-pol.): solid; cross-polarization (X-pol.): dashed.)

Full-wave simulations were performed in HFSS. Fig. 3(a) shows the simulated *H*-plane magnitude of the electric field at 30 GHz for Port 6, where an approximately planar wavefront is observed across the radiating aperture. Beams associated with ports on opposite sides can degrade due to coupling and physical blockage; to mitigate this effect, the two edge ports are designated as virtual ports. Fig. 3(b) shows the simulated radiation patterns of Port 6 at 26 GHz, 30 GHz, and 32 GHz, with peak gains of 13.6 dBi, 14.2 dBi, and

This article has been accepted for publication in IEEE Antennas and Wireless Propagation Letters. This is the author's version which has not been fully edited and content may change prior to final publication. Citation information: DOI 10.1109/LAWP.2025.3631510

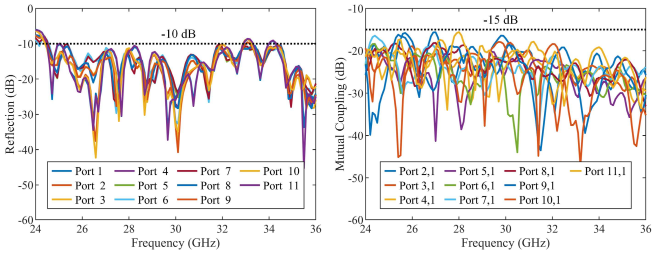

(a) (b)

Fig. 4. Simulated (a) reflection and (b) mutual coupling of a single-lens element's feed ports.

13.6 dBi, respectively. Fig. 4 shows that the simulated feed-port reflection and mutual coupling are below −10 dB and −15 dB across 26–32 GHz.

C. Array Synthesis and Beam Scanning

In the proposed hybrid array, ten planar Luneburg lens elements are uniformly spaced 6 mm apart along the y-axis, forming a one-dimensional array. Beam steering is performed in the *E*-plane. Owing to mutual coupling, the response of an embedded element in an array differs from that of a single element; therefore, embedded-element patterns and gains were used for array synthesis and performance prediction [20]. The embedded element pattern at 30 GHz was obtained from full-wave simulations using HFSS. For the unscanned case, *H*-plane array patterns for each port-switched beam were synthesized using uniform amplitude weighting. For *E*-plane scanning, array patterns were calculated for scanning angles ranging from −30° to 30° in 10° increments, using phase-only control across the array.

III. FABRICATION, MEASUREMENT, AND DISCUSSION

A. Antenna Fabrication

The proposed planar Luneburg lens was fabricated using a standard PCB process on a RO4350B substrate with a thickness of 1.524 mm. The lens and feed were integrated on a single PCB layer to reduce assembly complexity and cost. The graded index was achieved using periodic NPVs produced by precision computer numerical control (CNC) drilling, with via diameters ranging from 0.3 to 1.2 mm. A matching layer was additively manufactured by an UltiMaker S3 3D printer using PLA material ($\varepsilon_r = 2.8$) [21] and mechanically secured to the lens aperture to minimize free-space reflections. To characterize the embedded element pattern, an embedded element test array was fabricated and assembled. Fig. 5(a) shows the fabricated hardware.

B. Measurement and Results

Both the single element and the embedded element in the test array were measured in an anechoic chamber, as shown in Fig. 5(b). S-parameters were measured using a vector network analyzer (Agilent N5224A), and radiation patterns were obtained with a planar near-field measurement system.

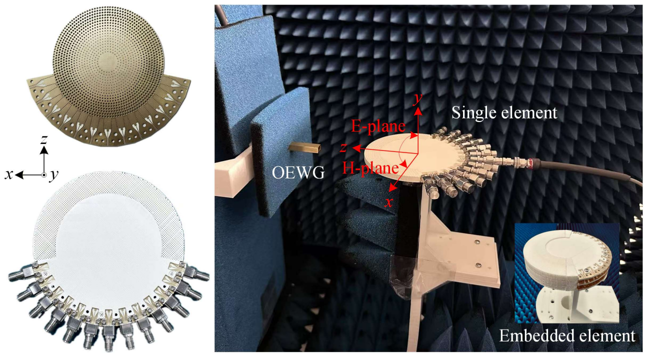

(a) (b)

Fig. 5. (a) Photographs of the fabricated planar Luneburg lens without (top) and with (bottom) a matching layer and connectors. (b) Photographs of the measurement setup. (OEWG: open-ended waveguide.)

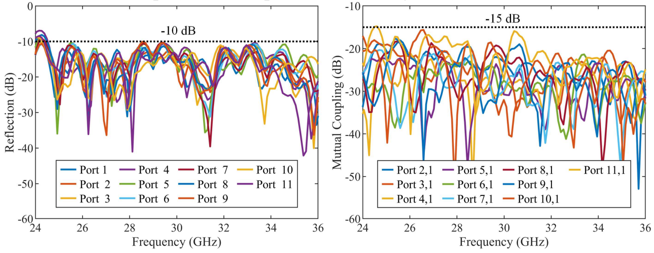

(a) (b)

Fig. 6. Measured (a) reflection and (b) mutual coupling of a single-lens element's feed ports.

TABLE I
COMPARISON OF MEASURED AND SIMULATED RADIATION PATTERN PARAMETERS AT 30 GHZ

Antenna Type		Gain (dBi) 0°	HPBW H/E 0°	X-pol. (dB) 0°	SLL (dB) H/E ±60°/±30°	SL (dB) H/E ±60°/±30°
Single Lens	Sim.	14.2	7.3° / 32.0°	-38	-8	0.6 / n.a.
	Mea.	13.4	8.0° / 29.2°	-26	-11	1.7 / n.a.
Hybrid Array	Sim.	23.2	6.7° / 8.5°	-21	-11	1.1 / 2.5
	Mea.	22.2	6.8° / 8.3°	-22	-8	2.4 / 2.9

Note: HPBW = half-power beamwidth; H/E = *H*-plane/*E*-plane; SLL = sidelobe level; SL = scan loss; Sim. = simulation; Mea. = measurement; n.a. = not available.

Table I summarizes the key parameters of measured and simulated patterns. Fig. 6 shows that the measured feed-port reflection and mutual coupling are below -10 dB and −15 dB across 26–32 GHz. Fig. 7(a)–(c) shows the radiation patterns, illustrating both co- and cross-polarization; the maximum measured cross-polarization is below −20 dB. Fig. 7(d) shows the peak gain and efficiency. From 26 to 32 GHz, the measured peak gain of Port 6 is 12.7–13.4 dBi (element) and 21.5–22.5 dBi (array); the measured aperture efficiency is 25%–37% (element) and 21%–35% (array); the measured radiation efficiency is 42%–50% (element) and 40%–44% (array). The maximum peak gain occurs at 27 GHz.

As expected, the embedded-element pattern exhibits noticeable distortion caused by mutual coupling. When there are no phase shifters and a feed network, array patterns synthesized from the embedded-element responses effectively approximate the array's radiation performance and scan behavior [20]. Fig. 8(a) shows the measured and simulated *H*-plane patterns of the hybrid array for the eleven port-switched beams at 30 GHz, while Fig. 8(b) shows the *E*-plane patterns for seven scanned beams at 30 GHz. The scan loss is less than 3 dB across all beams.

This article has been accepted for publication in IEEE Antennas and Wireless Propagation Letters. This is the author's version which has not been fully edited and content may change prior to final publication. Citation information: DOI 10.1109/LAWP.2025.3631510

TABLE II
COMPARISON WITH REPORTED 3D LUNEBURG LENS, HYBRID LENS ARRAYS, AND PHASED ARRAYS

Ref.	**Antenna Type**	**Realization**	**Freq.**	**IFBW**	**Peak Gain**	**SR (H/E)**	**SL (H/E)**	**SLL**	**Aperture Efficiency**	**Pol.**	**X-Pol.**
[2]	3D LL	3D printing rings	33 GHz	40%	21.2dBi	±61° / 0°	2.5 / n.a.	-15dB	35%–49%	LP	n.a.
[4]	3D LL	Perforated slices	27.5 GHz	40%	28.5 dBi	0° / 0°	n.a.	-15dB	22%–50%	LP	-15 dB
[5]	HLA	Metal milling	60 GHz	10%	22.5 dBi	±55° / ±30°	1 dB / 2.8 dB	-10 dB	40%	LP	n.a.
[8]	HLA	Single-layer PCB	9.2 GHz	27%	15.3 dBi	±40° / ±44°	3.4 dB / 3 dB	-10 dB	n.a.	LP	-15 dB
[23]	PA	Multilayer PCB	26.5 GHz	64%	22.3 dBi	±36° / ±36°	3 dB / 3 dB	-10 dB	77%	CP	n.a.
[24]	PA	Double-layer PCB	29 GHz	12%	22.0 dBi	±60° / ±60°	4.5 dB / 4.5 dB	-7 dB	57%	CP	n.a.
This Work	HLA	Single-layer PCB	30 GHz	21%	22.2 dBi	±60° / ±30°	2.4 dB / 2.9 dB	-8 dB	21%–35%	LP	-20 dB

Note: Ref. = reference; Freq. = frequency; IFBW = impedance fractional bandwidth; SR = scan range; Pol. = polarization; LP = linear polarization; CP = circular polarization; LL = Luneburg Lens; HLA = Hybrid lens array; PA = phased array.

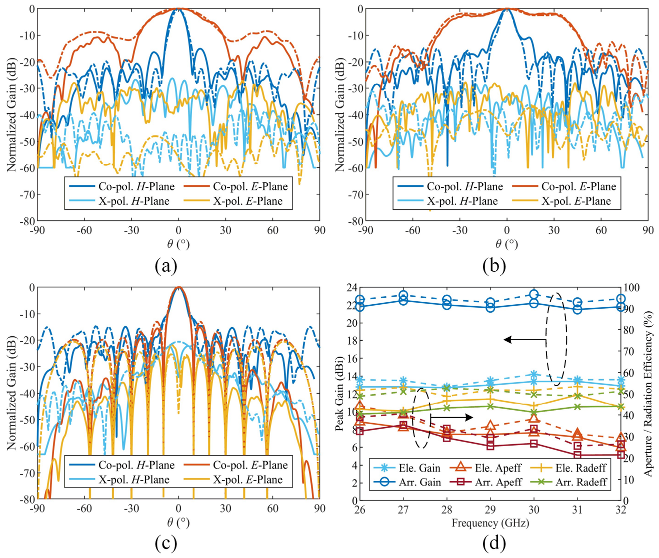

(a) (b)

(c) (d)

Fig. 7. Measured (solid) and simulated (dashed) radiation patterns for Port 6 at 30 GHz: (a) single element, (b) embedded element, and (c) array. (d) Measured (solid) and simulated (dashed) peak gain, aperture efficiency, and radiation efficiency of the single element and the array for Port 6 over 26–32 GHz. (Ele. = Element; Arr. = Array; Apeff = Aperture efficiency; Radeff = Radiation efficiency.)

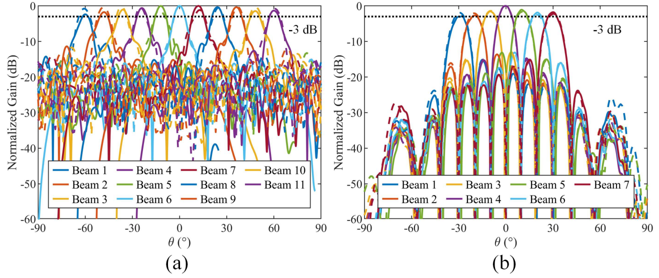

(a) (b)

Fig. 8. Measured (solid) and simulated (dashed) radiation patterns of the hybrid array at 30 GHz: (a) *H*-plane (port-switched beams) and (b) *E*-plane (scanned beams).

C. Discussion and Comparison

The measured results are in good agreement with the full-wave simulations, validating the proposed design. The element radiation patterns exhibit the expected narrow *H*-plane and wide *E*-plane beamwidths, consistent with simulation. The array offers wide-angle coverage of ±60° in the *H*-plane and ±30° in the *E*-plane. The primary factors limiting gain are free-space reflections and the dielectric loss of the PLA. Increasing the substrate thickness and reducing the size of the matching layer can effectively improve aperture efficiency.

The remaining discrepancies are mainly caused by (i) planar near-field truncation from the finite scan aperture, (ii) measurement alignment errors, and (iii) tolerances in the fabrication and assembly of the matching layer. In planar near-field measurements, the scan aperture should be larger than the field extent to prevent edge truncation [22]. In our setup, the sampling angle range is ±75°, which causes truncation and spectral leakage during the spatial transformation, reducing far-field accuracy at large theta angles. Nonetheless, the data is sufficient for evaluation and closely matches the simulations in the main beam and near-in sidelobes.

Table II compares the proposed design with other reported designs. The proposed offers broadband operation, high gain, and wide-angle beam coverage with comparatively low scan loss. Compared to traditional 3D lenses [2], [4] and previous hybrid lens arrays [5], the proposed architecture achieves monolithic feed-lens integration on a single-layer PCB, which is easily compatible with mm-wave circuitry and allows low-cost, large-scale manufacturing. Compared with hybrid lens arrays in [8], this design provides higher gain in a more compact size. Compared to phased arrays [23], [24], it offers lower scan loss, lower cost, and lower power consumption. In summary, the proposed hybrid lens array achieves a good balance between performance and cost/power efficiency.

V. CONCLUSION

This letter demonstrated a cost- and power-efficient hybrid array architecture based on planar Luneburg lens elements with integrated GCPW-to-SIW feeds on a single-layer PCB. A planar lens element was fabricated and validated over the 26–32 GHz band. A ten-element array was evaluated at 30 GHz, achieving a measured peak gain of 22.2 dBi. Beam switching covered ±60° in the *H*-plane with scan loss less than 2.4 dB, and beam scanning covered ±30° in the *E*-plane with scan loss less than 2.9 dB, while sidelobe levels remained below −8 dB across all beams. Compared to conventional phased arrays, the proposed approach reduces cost and power consumption without sacrificing scanning performance. The hybrid architecture is ideal for large-scale deployment in 6G systems.

This article has been accepted for publication in IEEE Antennas and Wireless Propagation Letters. This is the author's version which has not been fully edited and content may change prior to final publication. Citation information: DOI 10.1109/LAWP.2025.3631510

REFERENCES

[1] K. F. Brakora, J. Halloran, and K. Sarabandi, "Design of 3-D Monolithic MMW Antennas Using Ceramic Stereolithography," *IEEE Trans. Antennas Propag.*, vol. 55, no. 3, pp. 790–797, Mar. 2007, doi: 10.1109/TAP.2007.891855.

[2] Y. Li, L. Ge, M. Chen, Z. Zhang, Z. Li, and J. Wang, "Multibeam 3-D-Printed Luneburg Lens Fed by Magnetoelectric Dipole Antennas for Millimeter-Wave MIMO Applications," *IEEE Trans. Antennas Propag.*, vol. 67, no. 5, pp. 2923–2933, May 2019, doi: 10.1109/TAP.2019.2899013.

[3] C. Wang, J. Wu, and Y.-X. Guo, "A 3-D-Printed Multibeam Dual Circularly Polarized Luneburg Lens Antenna Based on Quasi-Icosahedron Models for Ka-Band Wireless Applications," *IEEE Trans. Antennas Propag.*, vol. 68, no. 8, pp. 5807–5815, Aug. 2020, doi: 10.1109/TAP.2020.2983798.

[4] S. Rondineau, M. Himdi, and J. Sorieux, "A sliced spherical Luneburg Lens," *IEEE Antennas Wireless Propag. Lett.*, vol. 2, pp. 163–166, 2003, doi: 10.1109/LAWP.2003.819045.

[5] P. Castillo-Tapia et al., "Two-Dimensional Beam Steering Using a Stacked Modulated Geodesic Luneburg Lens Array Antenna for 5G and Beyond," *IEEE Trans. Antennas Propag.*, vol. 71, no. 1, pp. 487-496, Jan. 2023, doi: 10.1109/TAP.2022.3217175.

[6] P. Castillo-Tapia, J. Rico-Fernández, and O. Quevedo-Teruel, "V-Band Monolithic Additive-Manufactured Geodesic Lens Array Antenna," *IEEE Antennas Wireless Propag. Lett.*, vol. 22, no. 10, pp. 2527–2531, Oct. 2023, doi: 10.1109/LAWP.2023.3294541.

[7] A. B. Numan, J.-F. Frigon, and J.-J. Laurin, "Printed W-Band Multibeam Antenna with Luneburg Lens-Based Beamforming Network," *IEEE Trans. Antennas Propag.*, vol. 66, no. 10, pp. 5614–5619, Oct. 2018, doi: 10.1109/TAP.2018.2860119.

[8] S. Lei, G. Wei, K. Han, T. Qiu, and M. Wang, "2-D Multibeam Leaky-Wave Antenna Based on Modified Luneburg Lens," *IEEE Antennas Wireless Propag. Lett.*, vol. 23, no. 5, pp. 1453–1457, May 2024, doi: 10.1109/LAWP.2024.3358816.

[9] C. Pfeiffer and A. Grbic, "A Printed, Broadband Luneburg Lens Antenna," *IEEE Trans. Antennas Propag.*, vol. 58, no. 9, pp. 3055–3059, Sep. 2010, doi: 10.1109/TAP.2010.2052582.

[10] M. Bosiljevac, M. Casaletti, F. Caminita, Z. Sipus, and S. Maci, "Non-uniform metasurface Luneburg Lens antenna design," *IEEE Trans. Antennas Propag.*, vol. 60, no. 9, pp. 4065–4073, Sep. 2012, doi: 10.1109/TAP.2012.2207047.

[11] A. Dhouibi, S. N. Burokur, A. de Lustrac, and A. Priou, "Compact Metamaterial-Based Substrate-Integrated Luneburg Lens Antenna," *IEEE Antennas Wireless Propag. Lett.*, vol. 11, pp. 1504–1507, 2012, doi: 10.1109/LAWP.2012.2233191.

[12] M. K. Saleem, H. Vettikaladi, M. A. S. Alkanhal, and M. Himdi, "Lens Antenna for Wide Angle Beam Scanning at 79 GHz for Automotive Short Range Radar Applications," *IEEE Trans. Antennas Propag.*, vol. 65, no. 4, pp. 2041–2046, Apr. 2017, doi: 10.1109/TAP.2017.2669726.

[13] X. Wang, Y. Cheng, and Y. Dong, "A Wideband PCB-Stacked Air-Filled Luneburg Lens Antenna for 5G Millimeter-Wave Applications," *IEEE Antennas Wireless Propag. Lett.*, vol. 20, no. 3, pp. 327–331, Mar. 2021, doi: 10.1109/LAWP.2021.3049432.

[14] Y. Su and Z. N. Chen, "A Flat Dual-Polarized Transformation-Optics Beam Scanning Luneburg Lens Antenna Using PCB-Stacked Gradient Index Metamaterials," *IEEE Trans. Antennas Propag.*, vol. 66, no. 10, pp. 5088–5097, Oct. 2018, doi: 10.1109/TAP.2018.2858209.

[15] C. Hua, X. Wu, N. Yang, and W. Wu, "Air-Filled Parallel-Planar Cylindrical Modified Luneberg Lens Antenna for Multiple-Beam Scanning at Millimeter-Wave Frequencies," *IEEE Trans. Microw. Theory Techn.*, vol. 61, no. 1, pp. 436–443, Jan. 2013, doi: 10.1109/TMTT.2012.2227780.

[16] O. Quevedo-Teruel, J. Miao, M. Mattsson, A. Algaba-Brazalez, M. Johansson, and L. Manholm, "Glide-Symmetric Fully Metallic Luneburg Lens for 5G Communications at Ka-Band," *IEEE Antennas Wireless Propag. Lett.*, vol. 17, no. 9, pp. 1588–1592, Sep. 2018, doi: 10.1109/LAWP.2018.2856371.

[17] R. K. Luneburg, *Mathematical Theory of Optics.* Providence, RI: Brown Univ. Press, 1944.

[18] F. Foglia Manzillo et al., "A Multilayer LTCC Solution for Integrating 5G Access Point Antenna Modules," *IEEE Trans. Microw. Theory Techn.*, vol. 64, no. 7, pp. 2272–2283, Jul. 2016, doi: 10.1109/TMTT.2016.2574313.

[19] D. Deslandes and K. Wu, "Accurate modeling, wave mechanisms, and design considerations of a substrate integrated waveguide," *IEEE Trans. Microw. Theory Techn.*, vol. 54, no. 6, pp. 2516-2526, June 2006, doi: 10.1109/TMTT.2006.875807.

[20] J. L. Allen, L. E. Brennan, S. A. Cohn, A. D. Fuhs, G. R. Larmat, and P. M. Woodward, "Phased Array Radar Studies," Lincoln Laboratory, MIT, Cambridge, MA, USA, Tech. Rep. No. 236(U), Nov. 1961.

[21] I. Kuzmanić, I. Vujović, M. Petković, and J. Šoda, "Influence of 3D printing properties on relative dielectric constant in PLA and ABS materials," *Prog. Addit. Manuf.*, vol. 8, pp. 703–710, Feb. 2023, doi: 10.1007/s40964-023-00411-0.

[22] IEEE Recommended Practice for Near-Field Antenna Measurements, IEEE Standard 1720-2012.

[23] S. Das et al., "A Flat-Panel 8 × 8 Wideband K-/Ka-Band Dual Circularly Polarized Phased Array Antenna for CubeSat Communications," *IEEE Trans. Antennas Propag.*, vol. 71, no. 5, pp. 4153–4166, May 2023, doi: 10.1109/TAP.2023.3255640.

[24] R. S. Hao, J. F. Zhang, S. C. Jin, D. G. Liu, T. J. Li, and Y. J. Cheng, "K-/Ka-Band Shared-Aperture Phased Array with Wide Bandwidth and Wide Beam Coverage for LEO Satellite Communication," *IEEE Trans. Antennas Propag.*, vol. 71, no. 1, pp. 672–680, Jan. 2023, doi: 10.1109/TAP.2022.3222091.